water

MDPI

Article

Effect of Hydrodynamic Loadings and Vorticity Distribution on a Circular Cylinder in a Narrow Channel

Truc Thi Thu Tran [1,*], Chia-Ren Chu [1] and Tso-Ren Wu [2]

[1] Department of Civil Engineering, National Central University, 300 Jhong-Da Road, Jhong-Li, Taoyuan 32001, Taiwan; crchu@cc.ncu.edu.tw
[2] Institute of Hydrological and Oceanic Science, National Central University, 300 Jhong-Da Road, Jhong-Li, Taoyuan 32001, Taiwan; tsoren@ncu.edu.tw
* Correspondence: ttruc667@gmail.com; Tel.: +886-900788420

Abstract

A large eddy simulation (LES) model, integrated with the volume of fluid (VOF) method, was employed to investigate hydrodynamic forces and vorticity distribution around a circular cylinder in a narrow channel. The simulated surface pressure and drag coefficient closely matched the experimental results from flume testing. The ratio of cylinder diameter to channel width is defined as the blockage ratio (*Br*). The effects of blockage on hydrodynamic loadings and vortex structures around the cylinder were examined through a series of numerical simulations. The results reveal that blockage ratios exceeding 20% significantly alter key flow characteristics, including the upstream and circumferential pressure coefficients, drag coefficient, lateral force coefficient, and Strouhal number. Higher blockage ratios enhance near-wall vortex formation and intensify shear layers. The vertical (Ω_y), streamwise (Ω_x), and spanwise (Ω_z) vorticity components all increase with *Br*, leading to stronger and more spatially extensive vortex structures near the bed, particularly in the form of horizontally elongated vorticity structures. These changes have important implications for structural stability and local scour. Overall, the findings contribute to the optimization of hydraulic structure design by highlighting the effects of channel confinement on flow-induced forces.

Keywords: large eddy simulation; narrow channel; blockage effect; hydrodynamic loadings; vorticity distribution

Academic Editor: Bommanna Krishnappan

Received: 19 June 2025
Revised: 28 July 2025
Accepted: 6 August 2025
Published: 9 August 2025

Citation: Tran, T.T.T.; Chu, C.-R.; Wu, T.-R. Effect of Hydrodynamic Loadings and Vorticity Distribution on a Circular Cylinder in a Narrow Channel. *Water* **2025**, *17*, 2366. https://doi.org/10.3390/w17162366

1. Introduction

Many bridges worldwide have suffered severe damage due to scour around bridge abutments, particularly local scour at piers and piles. According to the AASHTO LRFD Bridge Design Specifications (2010), scour is considered a critical factor in the design of bridge foundations, especially under extreme event limit states. In a comprehensive review, Brandimarte et al. [1] concluded that flooding and foundation scour are among the most frequent contributors to bridge collapse, as supported by several earlier studies [2–5]. This finding is also supported by a review conducted by Zhang et al. [6], who analyzed global studies on bridge failures from 1980 to 2016. As illustrated in Figure 1, their results confirm that hydraulic causes, including scour, represent one of the leading external causes of bridge failure globally.

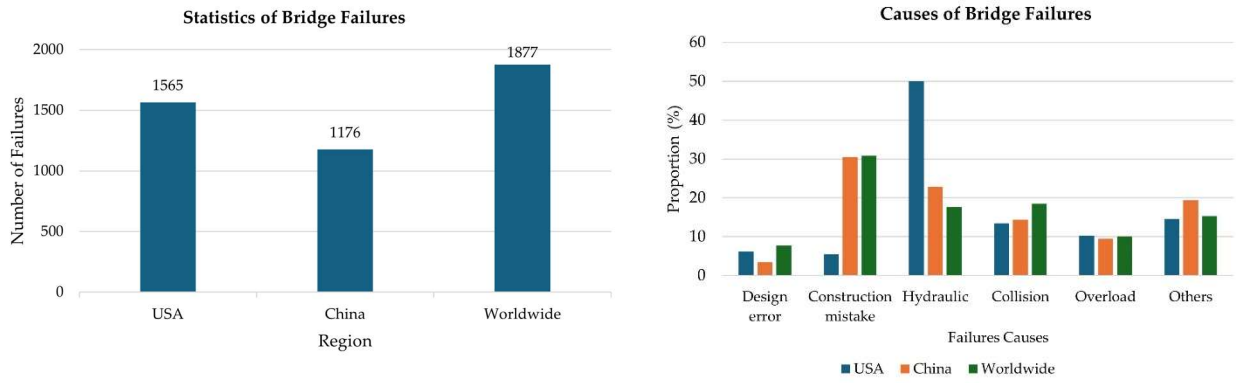

(**a**) (**b**)

Figure 1. Bridge failure statistics (1980–2016) by region and cause: (**a**) documented bridge failures by region (USA, China, and worldwide); (**b**) distribution of typical bridge failure causes [6].

Research on local scour has a long history, originating from field observations and laboratory experiments that systematically investigated the flow structures around the bridge piers and characterized the vortex patterns generated by cylindrical constructions in flume conditions. This is illustrated by Dargahi [7], who used flume experiments and hydrogen bubbles to visualize the vortex structures around a circular cylinder in a flat channel bed. The study demonstrated that the upstream horseshoe vortex system is the primary driver of scour around the pier. Simpson [8] reviewed the studies on junction flows that occur near an obstacle and a flat for laminar- and turbulent-approaching boundary layers. The review concluded that the pressure gradient surrounding the obstacle creates a three-dimensional separation, allowing development into horseshoe vortices. Das et al. [9] used an acoustic Doppler velocimeter to measure the vorticity fields around different pier shapes, including square, circular, and equilateral triangular piers, under clear-water equilibrium scour conditions with a uniform sand bed. The results demonstrated that the square and equilateral triangular pier produced stronger circulation and more concentrated vorticity within the horseshoe vortex, particularly at azimuthal planes of 0° and 45°, compared to the circular pier under equilibrium scour conditions. Gautam et al. [10] compared velocity measurements around a simple circular pier and a complex pier composed of a column, an elliptical pile cap, and multiple piles. They observed that the flow fields differed significantly between the two pier types, with reverse flow prevailing downstream of the simple pier at low Reynolds numbers (*Re*) and shifting upstream as the *Re* increased.

Alongside experimental studies, computational fluid dynamics (CFD) models have been applied to investigate the horseshoe vortex around a bed-mounted cylinder. Olsen and Melaaen [11] and Olsen and Kjellesvig [12] were among the first to use three-dimensional numerical models to simulate steady flow over a circular cylinder on a mobile bed, where sediment transport and bed evolution were considered by coupling the flow field with sediment continuity and utilizing the standard k-ε model and a finite volume approach. Their results agreed well with the physical model tests [13]. On the other hand, Tseng et al. [14] used a weakly compressible large eddy simulation (LES) model to investigate the three-dimensional flow field around square and circular cylinders on an immobile bed, i.e., a non-erodible rigid surface. Their findings showed that the down-welling flow in front of the cylinder generated a horseshoe vortex. Escauriaza and Sotiropoulos [15] applied the detached eddy simulation (DES) model to examine the effect of Re on the horseshoe vortex in the junction of the cylinder and channel bed. Their simulation results highlighted that the horseshoe vortex in front of the cylinder was composed of a train of several vortical

structures and was affected by Re, as demonstrated by the three-dimensional visualization of coherent structures and instantaneous image of vorticity at the symmetry plane. In a combined numerical and experimental approach, Kirkil and Constantinescu [16] employed LES modeling and laboratory experiments to visualize the turbulent horseshoe vortex and the near-wake flow behind a circular cylinder on a flat bed under subcritical (Re = 16,000) and supercritical ($Re = 5 \times 10^5$) shallow channel conditions. Their analysis indicated that a single primary necklace vortex dominated the horseshoe vortex region in both flow regimes, while bimodal oscillations within the vortex core enhanced turbulent kinetic energy and Reynolds stresses.

In addition to investigations of the horseshoe vortex formed in front of a cylindrical pier in an open channel, another area of interest is the analysis of hydrodynamic forces acting on a cylinder placed in narrow open channel flows. In a study by Ranga Raju et al. [17], laboratory experiments were combined with theoretical analysis to examine the afflux, i.e., the increase in the upstream water level resulting from an obstruction, caused by three circular cylinders in open channel flows with various blockage ratios under subcritical conditions. Their findings indicated that the drag coefficient increased due to the blockage effect, leading to a decrease in the upstream free surface level, known as afflux. Davis et al. [18] quantitatively examined the impact of channel walls on the flow around a two-dimensional square cylinder constrained in a channel. They concluded that the blockage effect considerably alters the flow field and increases the drag coefficient and Strouhal number. Chu et al. [19] used an LES model to investigate the free-surface flows over a submerged rectangular bridge deck. Their study revealed that the drag coefficient remained constant when the blockage ratio was less than 14% but increased as the blockage ratio became larger than 14%. Furthermore, Chu et al. [20] and Nguyen and Lei [21] utilized CFD simulations to analyze the flow around circular cylinders, emphasizing the amplification of dynamic pressure and drag forces, particularly under confined flow conditions with varying Reynolds numbers. The blockage ratio refers to the ratio of the projected area of the cylinder to the cross-sectional area of the flow domain. These studies enhance the current understanding of how blockage ratio, cylinder geometry, and flow characteristics interact across diverse hydrodynamics environments.

More recently, Hurtado-Herrera et al. [22] conducted a numerical investigation using an LES model to examine the effects of blockage ratio (Br) and approach velocity on local scour around a vertical cylinder under clear-water and live-bed conditions. They compared two blockage ratios, Br = 0.0625 and 0.1, and found that both the scour rate and depth increased in the narrower channel due to stronger flow contraction. In their study, a channel was considered narrow when $Br \geq 0.1$, a condition that led to significant flow confinement and altered wake structures. Their results were validated against experimental data from [23,24], confirming the accuracy of the modeled horseshoe vortex-induced scour mechanisms. The LES-derived flow patterns and near-bed shear stress distributions revealed modifications of vortex structures induced by blockage. These findings contribute to the understanding of morphodynamic responses under confined conditions. However, there remains a need to quantify hydrodynamic loadings (e.g., drag and lift coefficients) and vorticity components (Ω_x, Ω_y, and Ω_z) across a range of Br to gain a deeper understanding of the interaction between flow characteristics and confinement effects in narrow-channel conditions.

In summary, previous experimental and numerical studies have contributed to the understanding of horseshoe vortex formation and hydrodynamic forces acting on cylindrical structures in open channel flows. However, most of these efforts have focused on wide channels and horizontally oriented cylinders, with limited attention being paid to confined flows and the three-dimensional vorticity components (Ω_x, Ω_y, and Ω_z) around vertically

mounted cylinders. Additionally, while local scour and flow separation have been widely studied, the systematic effects of *Br* on hydrodynamic loads and vortex development remain insufficiently explored. The present study addresses these gaps by employing an LES model to investigate the influence of *Br* (ranging from 10% to 30%) on vorticity distribution and hydrodynamic forces in narrow-channel flows. In this context, a narrow channel refers to a flow domain in which lateral sidewalls significantly affect the local hydrodynamics, typically corresponding to $Br > 10\%$. The blockage ratio is defined as follows:

$$Br = \frac{D}{W} \tag{1}$$

where D and W are the cylinder diameter and the channel width, respectively. The findings of this study aim to support the design and safety assessment of hydraulic structures operating under confined flow conditions, where flow constriction can substantially modify velocity fields, vortex dynamics, and hydrodynamic loading.

2. Numerical Model

This study combined a three-dimensional LES model with the VOF method to simulate the hydrodynamic loadings and vorticity distributions in confined channel flows with a range of widths. The numerical solver was modified from the open-source code Truchas, which was developed by Los Alamos National Laboratory [25]. The same numerical simulation has been employed to predict the free surface flow over a rectangular deck [19], dambreak flows over cylinder arrays [26], and the flow field around a cross-river rubber dam [27].

The filtered continuity equation and Navier–Stokes equations can be used to model fluid motion [28,29]:

$$\frac{\partial \overline{u_i}}{\partial x_i} = 0 \tag{2}$$

$$\frac{\partial \rho\, \overline{u_i}}{\partial t} + \frac{\partial \rho \overline{u_i u_j}}{\partial x_j} = -\frac{\partial \overline{P}}{\partial x_i} + \rho g \delta_{i3} + \frac{\partial}{\partial x_j}\left[\mu_{eff}\left(\frac{\partial \overline{u_i}}{\partial x_j} + \frac{\partial \overline{u_j}}{\partial x_i}\right)\right] \tag{3}$$

where u, P, ρ, and g are the fluid velocity, pressure, density of fluid, and gravitational acceleration, respectively, and the over-bar indicates that the quantity is the spatially filtered value [30,31]. The subscripts i, j = 1, 2, and 3 represent the x, y, and z directions, respectively; t is the time; δ is the Kronecker delta; and μ_{eff} is the effective viscosity, which is represented by

$$\mu_{eff} = \mu + \mu_{SGS} \tag{4}$$

where μ is the dynamic viscosity of the water and μ_{SGS} is the viscosity of the sub-grid scale turbulence. The sub-grid scale turbulence was modeled using the Smagorinsky formula [32]:

$$\mu_{SGS} = \rho(C_s \Delta_s)^2 \left[2\overline{S}_{ij}\overline{S}_{ij}\right]^{1/2} \tag{5}$$

where C_s and S_{ij} are the Smagorinsky coefficient and the filtered rate of strain, respectively [33]:

$$\overline{S}_{ij} = \frac{1}{2}\left(\frac{\partial \overline{u_i}}{\partial x_j} + \frac{\partial \overline{u_j}}{\partial x_i}\right) \tag{6}$$

Δ_s is the characteristic length of the spatial filter. The characteristic length is calculated as follows:

$$\Delta_s = (\Delta x \Delta y \Delta z)^{1/3} \tag{7}$$

In the numerical simulation, the value of the Smagorinsky coefficient was set to $C_s = 0.15$ based on our previous research [20,27,34,35]. The projection approach [36] was

employed to solve the Poisson pressure equation and to decouple the velocity and pressure in the Navier–Stokes equations. The VOF method [37] was used to resolve the kinematics of the water surface. The volume fraction f_m of water in a grid cell is governed by the following equation:

$$\frac{\partial f_m}{\partial t} + \frac{\partial}{\partial x_j}\left(f_m \overline{u_j}\right) = 0 \tag{8}$$

When $f_m = 1$, $f_m = 0$, or $0 < f_m < 1$, the computational cell is full of water, the cell is fully occupied by air, or the cell is partially occupied by water, respectively. The convergence criterion for the momentum equation was set to 10^{-6}, and the Courant number was Cr = 0.85. The average time step was 1×10^{-3} s, and the output time step was $\Delta t = 0.1$ s. The simulation results before dimensionless time $\tau = tV_1/D = 30$ were discarded to exclude the initial transient results of the simulation, where V_1 and D are the upstream velocity and the cylinder diameter, respectively. The time-averaged velocity and pressure were computed from the simulation results when the dimensionless time τ = 30–64.

3. Model Validation

The accuracy of the present numerical model was validated by comparing its simulation results with the laboratory experiments conducted by Dargahi [7]. A circular cylinder with a diameter and a height of D = 0.15 m and 0.50 m, respectively, was installed along the centerline of a water flume. The upstream and downstream water depth was h_1 = 0.2 m. Figure 2 presents the schematic of the computational domain and flow conditions. The domain was 3.15 m, 1.5 m, and 0.36 m in length, width, and height and was discretized using the finite volume method. The channel bed and sidewalls were set as no-slip boundary conditions, and the downstream boundary was defined with a zero-velocity gradient, following practices adopted in previous OpenFOAM-based simulations [38,39]. The domain was initialized with water, and a velocity field based on the inlet log-law profile was applied as the initial condition to represent a fully developed flow throughout.

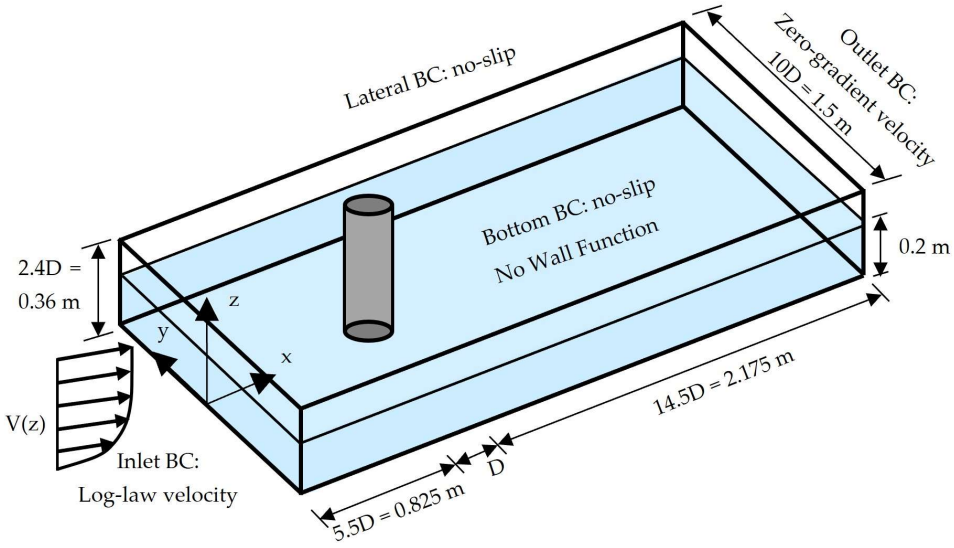

Figure 2. Schematic diagram of the flow condition, where the cylinder diameter D = 0.15 m.

A logarithmic profile was used to describe the distribution of streamwise velocity in the vertical direction:

$$\frac{V(z)}{u_*} = \frac{1}{\kappa} ln\left(\frac{z}{z_0}\right) \tag{9}$$

where the von Karman constant, shear velocity, and roughness length are κ = 0.41, u^* = 0.012 m/s, and $z_0 = 2.5 \times 10^{-5}$, respectively [7]. Note that the grid size of Δz = 2–3 mm

near the bottom wall can be normalized as $z+ = \Delta z u^*/\nu$ = 24–36, which is slightly larger than the thickness of the viscous sublayer. Since the viscous sublayer is not resolved and the study focuses on large-scale flow dynamics, this wall treatment is considered appropriate, in accordance with previous LES studies [40–42]. The reference velocity at z = 0.18 m, y = 0, and 0.3 m from the inlet (from the cylinder face) was V_1 = 0.26 m/s; this velocity value will be used for validation grids. The upstream Froude number was $Fr_1 = V_1/(gh_1)^{0.5}$ = 0.186; the Reynolds number, based on the cylinder diameter, was $Re = V_1 D/\nu$ = 39,000.

A three-dimensional view of the computational mesh is shown in Figure 3a. The entire computational domain was divided into ten zones. The circular cylinder was located in Zone VI, with a non-structured grid (as depicted in Figure 3b). Zone V used a uniform grid, while the other zones utilized non-uniform grids with a stretching ratio of 1.05. The grid arrangement in the z direction was divided into two layers: finer grid cells (Δz = 3 mm for Grid 1, and Δz = 2 mm for Grid 2) in the lower layer (z = 0–30 mm) and a non-uniform grid in the upper layer (z = 30–200 mm). The vertical grid size was gradually increased (with a stretching ratio of 1.05). In the horizontal direction, the smallest grid size around the cylinder was 5 mm = $D/30$.

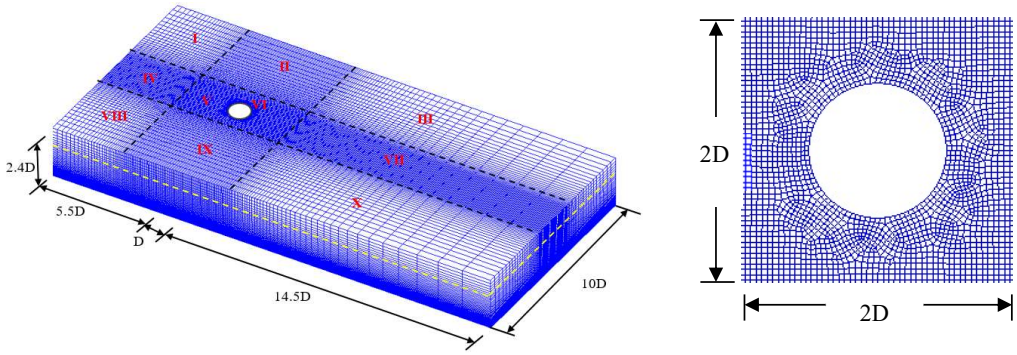

(**a**) Three-dimensional view of the computational mesh. (**b**) Mesh around the circular cylinder.

Figure 3. Computational domain and mesh arrangement. (**a**) Three-dimensional view where the yellow dashed line represents the still water depth. (**b**) Top view of the mesh around the cylinder.

Figure 4 compares the simulated velocity profiles at the upstream boundary (x/D = 2, y/D = 0) with the measured velocity distribution from Dargahi [7]. The curve was determined using the logarithmic profile in Equation (9). The average relative difference between the simulated and experimental results was 4.9% and 4.7% for Grid 1 and Grid 2, respectively. For the validation case, the *Br* was 10%. The simulated and measured pressure coefficients right in front of the cylinder (at x/D = 5.46, y/D = 0) are shown in Figure 5.

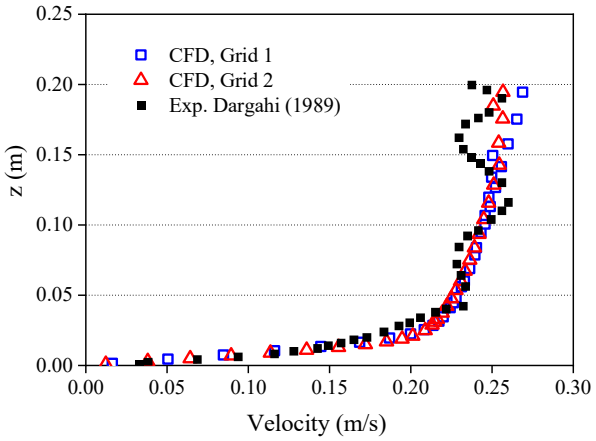

Figure 4. Velocity profile at the inlet boundary (at x/D = 2 and y/D = 0) for the experimental case [7].

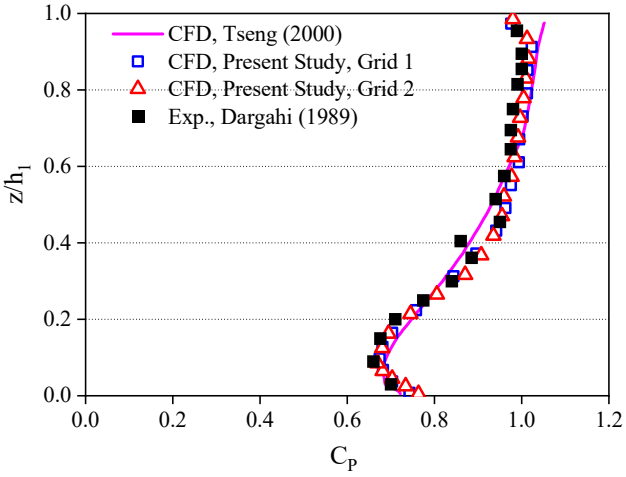

Figure 5. Comparison of simulated and measured pressure coefficients on the frontal side of the circular cylinder [7,14].

The pressure coefficient (C_p) is defined as follows:

$$C_p = \frac{P - P_s}{\frac{1}{2}\rho V^2} \tag{10}$$

where P is the total pressure, P_s is the hydrostatic pressure, ρ is the water density, and V is the streamwise velocity at height z = 0.18 m.

Figure 5 shows the distribution of C_p in front of the cylinder face (at x/D = 5.46, y/D = 0), which is directly related to the non-uniform velocity profile upstream of the cylinder. C_p is calculated using Equation (10). The average differences between the simulated and measured C_p values from Dargahi [7] are 2.18% and 2.1% for Grid 1 and Grid 2, respectively, while the discrepancy between the earlier study by Tseng [14] and Dargahi [7] is 3%. The good agreement between the measured and simulated C_p on the frontal side of the cylinder demonstrates the accuracy and reliability of the current LES model.

The time-averaged drag force and lateral force were calculated from the simulated pressure on the surface of the cylinder:

$$F_D = \sum_{j=1}^{m}\sum_{i=1}^{n} P(\theta_{i,j}) \cos\theta_{i,j} (R\Delta\theta)\Delta z \tag{11}$$

$$F_L = -\sum_{j=1}^{m}\sum_{i=1}^{n} P(\theta_{i,j}) \sin\theta_{i,j} (R\Delta\theta)\Delta z \tag{12}$$

where $\theta_{i,j}$ is the angle; R is the radius of the cylinder; n is the number of grid points on the cylinder surface; and m is the number of grid points in the z-direction. The current computation uses n = 90 (90 grid points around circumference of the cylinder) and m = 9 (9 different heights in the vertical direction). The drag coefficient, C_D, is defined as

$$C_D = \frac{F_D}{\frac{1}{2}\rho V^2 A} \tag{13}$$

where F_D is the drag force acting on the cylinder and $A = hD$ is the projected area of the circular cylinder. The lateral force coefficient, C_L, can be written as

$$C_L = \frac{F_L}{\frac{1}{2}\rho V^2 A} \tag{14}$$

where F_L is the lateral force acting on the cylinder.

Table 1 compares the drag coefficients and the Strouhal number computed by two different computational grids. The time-averaged drag coefficients C_D = 1.099 and 1.199 for Grid 1 and Grid 2, respectively, are very close to C_D = 1.10–1.20 of the two-dimensional circular cylinder in the range $10^3 < Re < 10^5$ [43–45]. The time-averaged lateral force coefficients are C_L = 0.06 and 0.04 for Grid 1 and Grid 2, respectively. They are close to the value C_L = 0 for a circular cylinder in uniform, symmetric flow. This comparison verifies the accuracy of the present LES model.

Table 1. Simulation results of the validation case using different computational grids.

Grid	Dargahi's Experiment	Grid 1	Grid 2
Total grid no.	-	949,326	1,562,615
Grid no. on the cylinder surface	-	90	120
Smallest grid size	-	Δx = 6 mm Δy = 6 mm Δz = 3 mm	Δx = 5 mm Δy = 5 mm Δz = 2 mm
Strouhal no.	0.20	0.206	0.208
Relative error	-	3.0%	4.0%
C_D	1.15	1.099	1.199
Relative error	-	4.43%	4.26%
C_L	0	0.06	0.04
CPU time	-	255 h	416 h

Note: Flow parameters: D = 0.15 m, h_1 = 0.2 m, V_1 = 0.26 m/s.

The Strouhal number (St) is computed as follows:

$$St = \frac{f_s D}{V} \tag{15}$$

where f_s is the shedding frequency. The shedding frequency was computed from the time series of lateral forces at a normalized height of z/h_1 = 0.6, resulting in frequencies of f_s = 33.6 Hz and 34.0 Hz for Grids 1 and 2, respectively. These values are in good agreement with previous results (St = 0.20–0.21) for two-dimensional circular cylinders at $Re = 10^3$–10^4 [46–48].

Figure 6 presents the simulated pressure coefficients around the cylinder at z/h_1 = 0.6 using two computational grids, along with experimental data for a two-dimensional circular cylinder ($Re = 4.4 \times 10^4$), as reported by Surry [49], which closely matches the Reynolds number of the present study. The good agreement between both datasets suggests that the flow fields at this height approximate two-dimensional behavior. According to potential flow theory, the theoretical C_p at the stagnation point (θ = 0°) is C_p = 1.0. The simulated values at this point are C_p = 0.991 and C_p = 0.986 for Grids 1 and 2, corresponding to deviations of 1% and 1.4%, respectively. Additionally, the experimental study [7] reported C_p = 0.965 at $\theta = 0°$, z/h_1 = 6, while the simulation by Tseng [14] yielded C_p = 0.97 (see Figure 5). This discrepancy arises because the velocity near the cylinder base is reduced by boundary layer effects, causing Cp to deviate from the theoretical value. Dargahi [7] also noted that the pressure gradients may be a result of the non-uniform velocity distribution in the approaching flow. Furthermore, the average total errors between the simulated results and the measurement of Surry [49] were 1.97% and 2.01% for Grids 1 and 2, respectively.

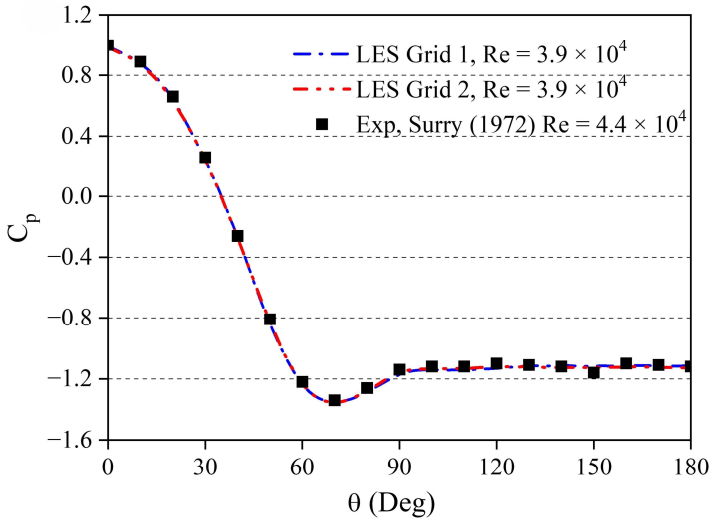

Figure 6. Validation of simulated pressure coefficients against experimental data on the cylinder surface at $z/h_1 = 0.6$ [49].

As shown in the numerical validation model, the results obtained using Grid 1 and Grid 2 show good agreement with the experimental data. This demonstrates that the present LES model can accurately simulate the flow field around the circular cylinder. It is worth noting that although both grids yielded comparable accuracy, the CPU time required for Grid 2 was longer than that of Grid 1 (see Table 1). Therefore, Grid 1 was selected for the remaining simulations in order to reduce computational cost.

4. Results and Discussion

4.1. Hydrodynamic Loading Effect

This section investigates the blockage effect on the hydrodynamic loadings and the vorticity distribution around a circular cylinder. The upstream and downstream water depths are identical, with $h_1 = 0.2$ m and the cylinder diameter $D = 0.15$ m. The upstream velocity profile is set to the same logarithmic profile as in the validation case, with a shear velocity of $u^* = 0.012$ m/s and a reference velocity $V_1 = 0.26$ m/s at height $z = 0.18$ m. The channel widths are set as $W = 1.5$ m, 1.05 m, 0.75 m, 0.6 m, and 0.5 m, resulting in $Br = 10\%$, 14.3%, 20%, 25%, and 30%, respectively.

Figure 7 illustrates the evolution of time-averaged velocity vectors around the circular cylinder at $z/h_1 = 0.04$ for various Br values. As the Br increases, the flow exhibits enhanced separation and a more pronounced recirculation zone in the cylinder's wake. Notably, the velocity in the gap between the cylinder and the sidewall increases significantly, and the velocity vectors become increasingly aligned with the channel walls. This behavior suggests a higher risk of erosion near the side boundaries and greater turbulence intensity downstream due to the confined flow. The observed changes in vector magnitude and direction underscore the impact of blockage on flow dynamics in narrow channels.

The time-averaged C_p on the frontal face of the cylinder (at $x/D = 5.46$, $y/D = 0$) under varying Br conditions is presented in Figure 8. As the channel width decreases, notable changes are observed in the C_p distribution along the cylinder surface. The minimum C_p consistently occurs at $z/h_1 = 0.1125$, and its magnitude decreases with increasing Br. The interaction between the incoming turbulent boundary layer and the cylinder surface is enhanced under more confined flow conditions. This implies that the Br influences the separation-induced vortex flow at the junction of the channel bed and the cylinder. Compared to the baseline case ($Br = 10\%$), the C_p value exhibits progressive deviations of 1.18%, 2.26%, 3.38%, and 5.61% at blockage ratios of 14.3%, 20%, 25%, and 30%, respectively.

These variations provide quantitative benchmarks for assessing the impact of *Br* on surface pressure characteristics in hydraulic structures.

The time-averaged C_p around the circumference of the cylinder at z/h_1 = 0.6 for different *Br* values is presented in Figure 9. As previously discussed in Figure 5, the frontal C_p (≈1.0) at $\theta = 0^\circ$ remains consistent for *Br* = 10% and 14.3% but becomes slightly greater than 1.0 when $Br \geq 20\%$. Beyond this threshold, the overall distribution of C_p around the cylinder undergoes a notable change. The values of C_p deviate from the potential flow theory, due to flow separation, at other locations along the cylinder circumference. In addition, the minimum C_p (θ = 68–80°) and the base pressure C_{pb} (θ = 120–180°) decrease with increasing *Br*, resulting from the high velocity in the gap region (see Figure 7). The location of minimum C_p is approximately at θ = 68° for *Br* = 10% and 14.3%, shifting toward the leeward side of the cylinder (θ = 76–80°) as *Br* increases. These results indicate that the blockage effect considerably alters the flow characteristics around the circular cylinder in an open channel.

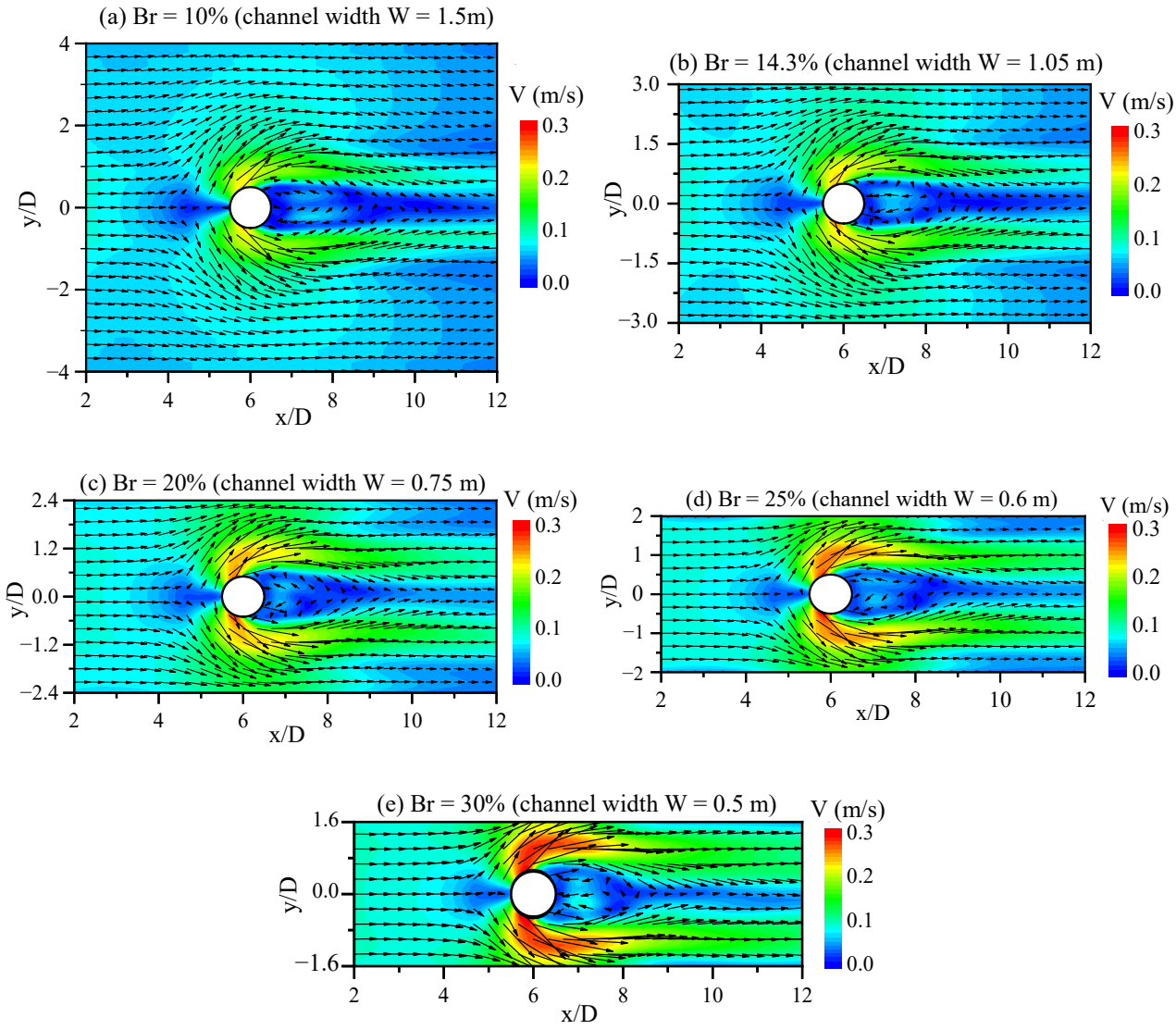

Figure 7. Time-averaged velocity vectors (at z/h_1 = 0.04) around the cylinder. (**a**) *Br* = 10%; (**b**) *Br* = 14.3%; (**c**) *Br* = 20%; (**d**) *Br* = 25%; (**e**) *Br* = 30%.

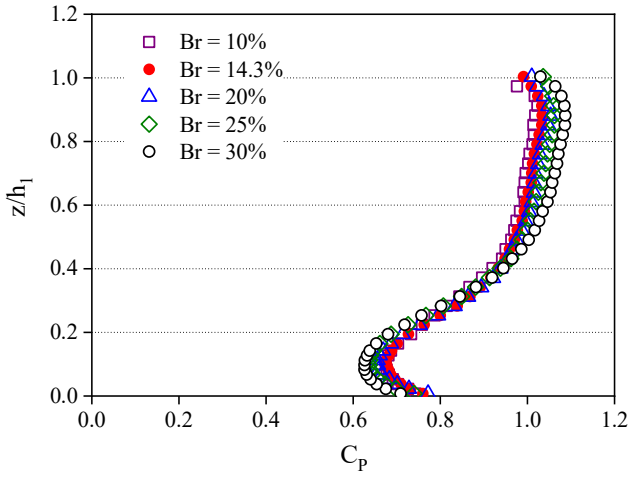

Figure 8. Time-averaged pressure coefficient on the frontal side of the circular cylinder (at x/D = 5.46 and y/D = 0).

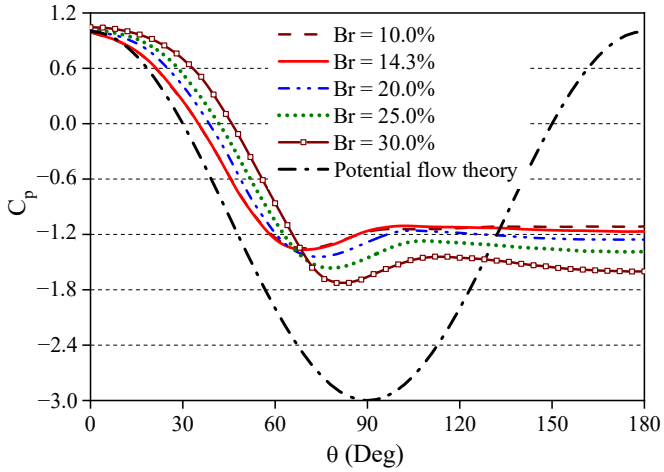

Figure 9. Time-averaged pressure coefficient on the cylinder surface at height z/h_1 = 0.6.

The time-averaged drag coefficients are plotted against *Br* in Figure 10. It shows that the C_D remains constant at C_D = 1.12 when $Br \leq 14.3\%$, indicating that *Br* has a negligible effect on drag under low-blockage conditions. This behavior is consistent with the results reported for circular cylinders in unconfined domains [14]. As *Br* increases, the blockage effect accelerates the incoming flow and increases the dynamic pressure on the front face of the cylinder, thereby amplifying the pressure difference between upstream and downstream surfaces and resulting in a higher C_D. This phenomenon was also observed by Chu et al. [19] for a horizontal rectangular cylinder in free surface flows. The contraction of the channel width not only contributed to the increase in C_D but also exerted a notable influence on C_L.

Figure 11 reveals the time histories of the lateral force coefficient for *Br* values ranging from 10% to 30%, computed using Equations (12) and (14). The results exhibit periodic fluctuations induced by vortex shedding around the cylinder. Higher blockage ratios, particularly *Br* = 25% and 30%, show significantly larger amplitudes and higher frequencies compared to lower-blockage conditions. This figure indicates that flow confinement intensifies the lateral forces acting on the cylinder, potentially leading to stronger dynamic responses and structural vibrations. These findings underscore the sensitivity of vortex-induced forces to geometric confinement in the flow domain. This is due to the enhanced vortex shedding, which makes the alternating low- and high-pressure zones become more

prominent and amplifies the lateral force oscillations. Consequently, an increase in the root mean square of C_L and St values can be anticipated, as shown in Figures 12 and 13.

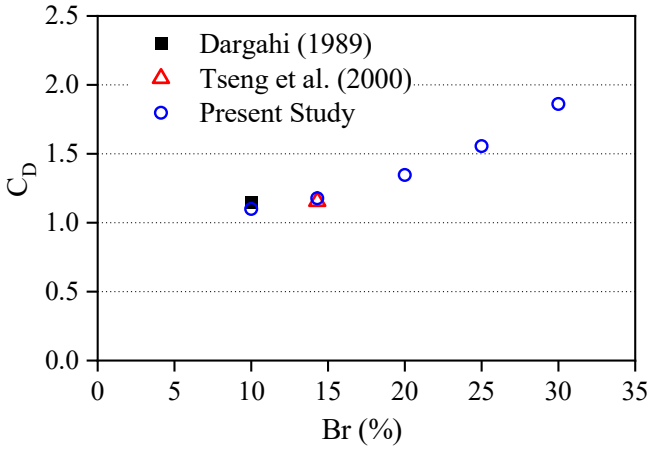

Figure 10. Relationship between the drag coefficient of circular cylinder and blockage ratios [7,14].

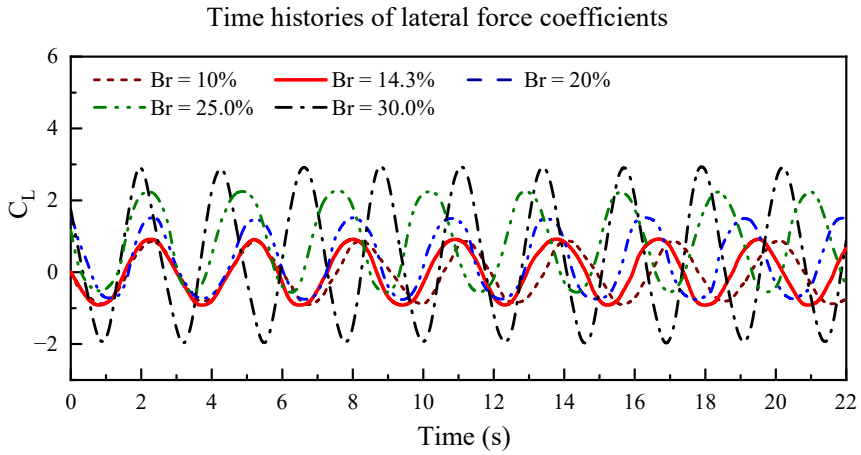

Figure 11. Time histories of lateral forces on the cylinder across a range of *Br*.

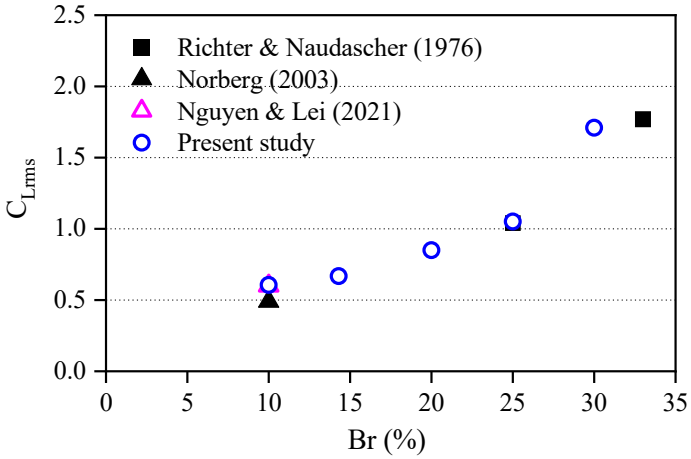

Figure 12. Effect of blockage ratio on the root mean square of the lateral force coefficient [21,50,51].

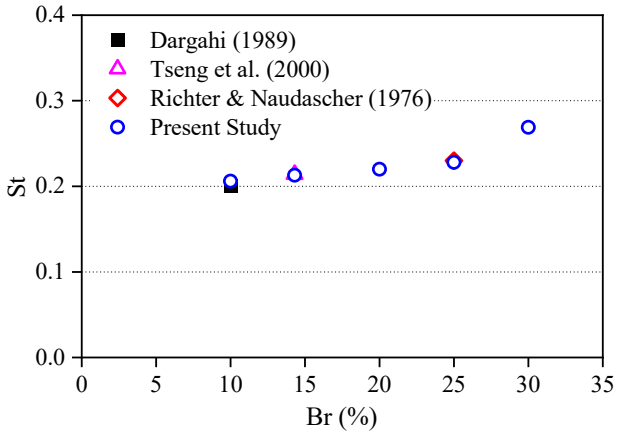

Figure 13. Relationship between the Strouhal number and blockage ratios [7,14,50].

The amplitude of the fluctuation is expressed as the root mean square value of the lateral force coefficient C_{L_rms}:

$$C_{L\_rms} = \sqrt{\frac{1}{N}\sum_{i=1}^{N}\left(C_L(t_i) - \overline{C}_L\right)^2} \quad (16)$$

where N = 228 is the data number and $\overline{C_L}$ is the time-averaged lateral force coefficient.

Figure 12 shows the variation in the root mean square of the lateral force coefficient for different blockage ratios. The values are derived from the temporal data shown in Figure 11 and calculated using Equation (16). A pronounced upward tendency in C_{L_rms} is observed as the *Br* increases, particularly within the range of 10% to 30%, indicating a stronger unsteady lateral force response under higher-confinement conditions. This trend confirms that greater flow confinement enhances vortex shedding intensity, which strengthens the alternating pressure field around the cylinder. As a result, the amplitude and persistence of unsteady lateral forces increase, leading to higher C_{L_rms} values. The diagram also compares the present results with previous experimental and computational studies [21,50,51], and the close agreement confirms the reliability of the current approach in capturing the effects of blockage on lateral force fluctuations. These results demonstrate that stronger and more coherent vortices, which are generated under high-blockage conditions, impose greater pressure asymmetry over time, thereby amplifying the overall lateral force acting on the cylinder.

The dimensionless *St* is plotted against *Br* in Figure 13. At *Br* = 10%, *St* = 0.206, which closely agrees with the experimental results [7,46]. In addition, the simulated value of *St* = 0.228 at *Br* = 25% is consistent with the findings of Richter and Naudascher [50], based on experiments involving a horizontal circular cylinder in a narrow rectangular duct. These comparisons support the validity of the LES model in investigating the effects of *Br* on hydrodynamic loading on circular obstacles in open channel flows. Moreover, Figure 13 shows that the *St* value increases when *Br* > 20%. This pattern results from the acceleration of flow through the narrowed gap caused by the reduced channel width, which amplifies the vortex shedding frequency and consequently elevates the *St* value.

As shown in the simulation results, variations in channel width under identical inlet flow conditions led to changes in hydrodynamic loadings. These findings are consistent with previous studies, underscoring the critical role of blockage in amplifying flow-induced scour and structural loading in narrow channels. Modifications in the pressure coefficient along the upstream surface and around the circumference of the cylinder at $z/h_1 = 0.6$, along with elevated drag coefficients, demonstrate the significant influence of *Br* on flow

behavior. Furthermore, the time history of C_L reveals a noticeable growth in oscillation amplitude at *Br* = 20–30%, resulting in higher values of both the C_{L_rms} and *St* values. These enhancements reflect intensified unsteady lateral forces acting on the structure. The diagrams illustrating these changes allow engineers to assess the impact of *Br* on structural performance and adapt their design plans accordingly.

4.2. Vorticity Distribution Effect

As well as the hydrodynamic loadings, this analysis also examines the vorticity distribution around the cylinder near the channel bed. Figure 14 is a schematic diagram of three-dimensional vorticity around the circular cylinder. The vorticity in Cartesian coordinates is

$$\vec{\Omega} = \left(\frac{\partial w}{\partial y} - \frac{\partial v}{\partial z}\right)\vec{i} + \left(\frac{\partial u}{\partial z} - \frac{\partial w}{\partial x}\right)\vec{j} + \left(\frac{\partial v}{\partial x} - \frac{\partial u}{\partial y}\right)\vec{k} \quad (17)$$

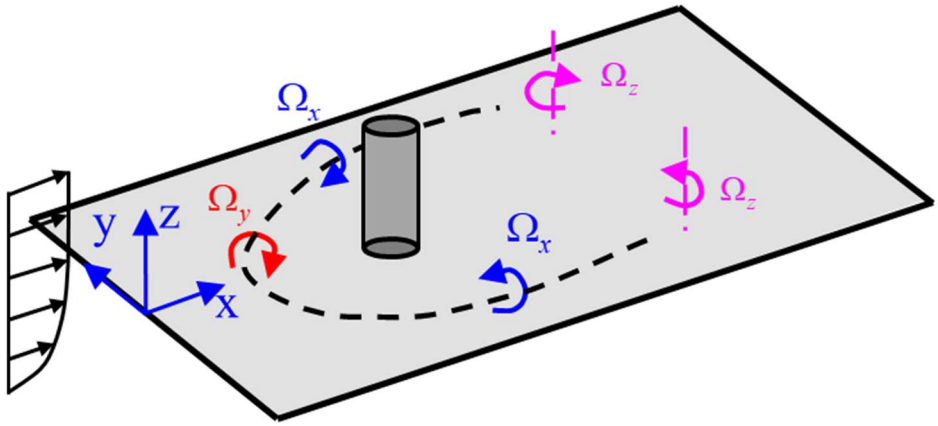

Figure 14. Schematic diagram of the horseshoe vortex around a circular cylinder in an open channel flow.

Vorticity upstream of a cylinder in unconfined channels has been the primary focus of previous studies. In contrast, the present study examines the influence of blockage on vertical vorticity in front of the cylinder and the streamwise vorticity component within the region between the sidewall and the cylinder, referred to hereafter as the gap region. Figure 15 shows the distribution of vertical vorticity (Ω_y) upstream of a wall-mounted cylinder for *Br* = 10–30%. The contours are plotted on the symmetrical plane (y = 0), highlighting the formation of near-wall vortical structures. In all cases, a strong concentration of Ω_y appears near the cylinder base, indicating intensified spanwise shear layers caused by the deflection of the incoming boundary layer. As the *Br* increases, both the peak vorticity and its closeness to the cylinder surface grow, suggesting stronger flow confinement and adverse pressure gradients. These changes imply that local scouring in front of circular piers may increase under narrow-channel conditions with erodible beds.

The relationship between the blockage ratio and the peak Ω_y on the symmetry plane (y = 0) is shown in Figure 16. The results show a consistent increase in peak vertical vorticity as Br increases from 10% to 30%, supporting the interpretation that geometric confinement intensifies upstream vortex generation by increasing adverse pressure gradients and boundary layer deflection near the cylinder base. The evolution in Ω_{y_max} values indicates the development of stronger near-bed shear layers and more complex three-dimensional vortex interactions at higher blockage ratios. These findings are consistent with previous studies [7,14,22,52] which reported that the obstacle in confined channel flows exhibits stronger shear-induced vorticity and more pronounced vortex deformation due to higher

pressure gradients and velocity contraction near the junction between the channel bed and the cylinder surface.

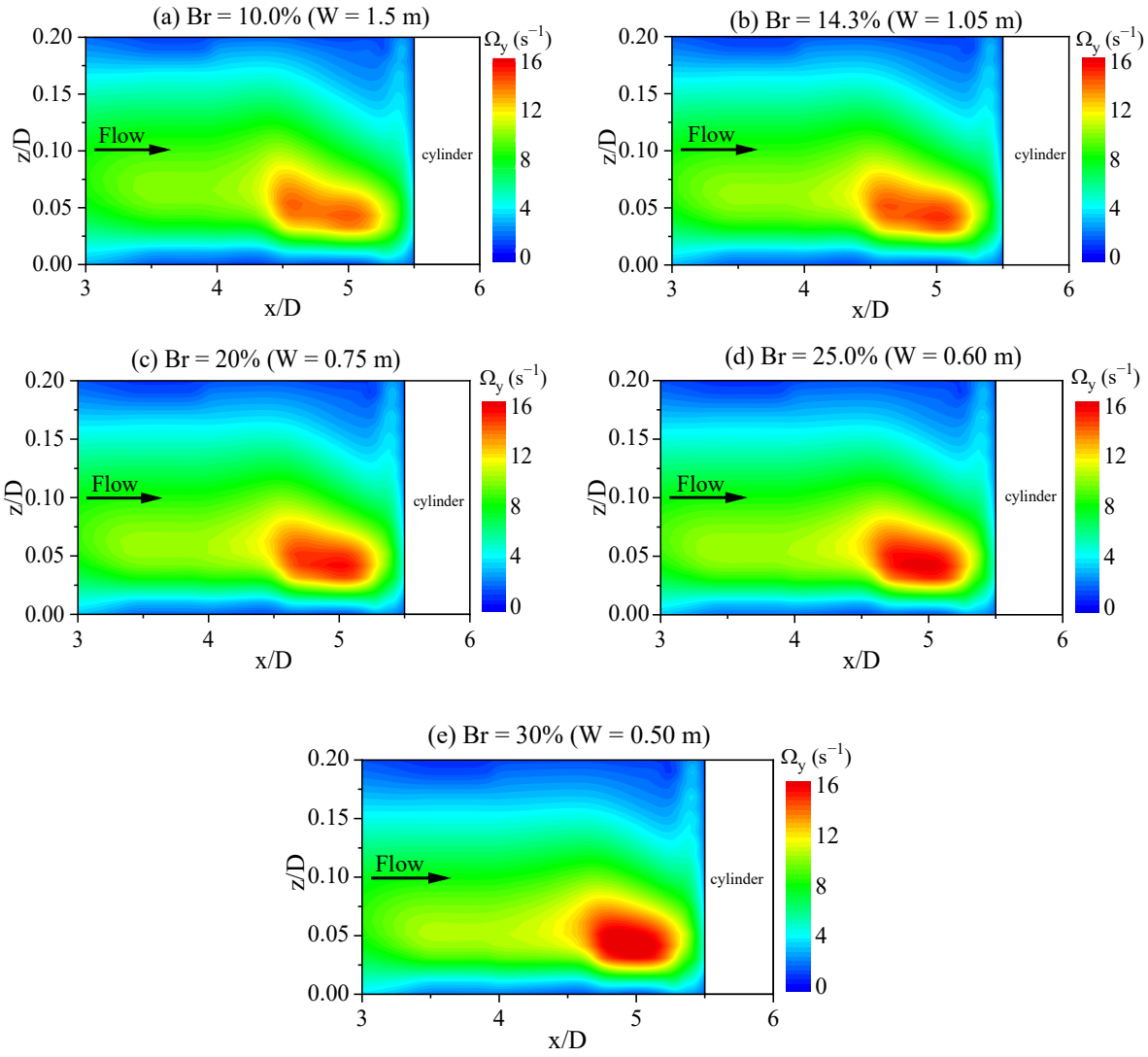

Figure 15. Distribution of the vorticity Ω_y on the symmetric plane ($y = 0$) of the cylinder at z/D = 0–0.2. (**a**) *Br* = 10%; (**b**) *Br* = 14.3%; (**c**) *Br* = 20%; (**d**) *Br* = 25%; (**e**) *Br* = 30%.

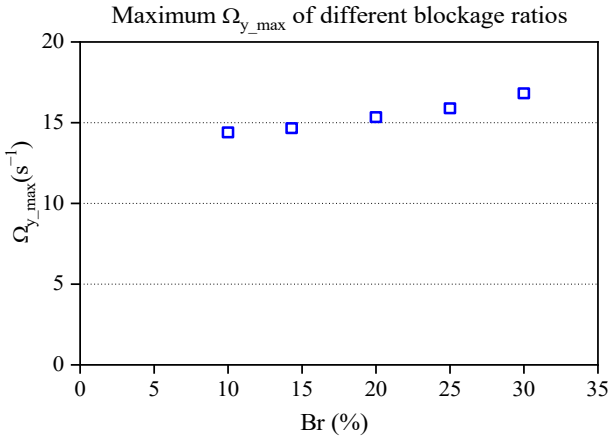

Figure 16. Maximum vorticity Ω_y in front of the cylinder on the symmetric plan ($y = 0$) of the cylinder.

Figure 17 illustrates the distribution of streamwise vorticity (Ω_x) on the y-z plane across the cylinder center at $x/D = 6$ under varying *Br* conditions. The vortex rotates coun-

terclockwise when the vorticity $\Omega_x > 0$ (represented by red color), whereas the vorticity $\Omega_x < 0$ (represented by blue color) indicates the vortex rotating clockwise. At Br = 10% and 14.3%, the vorticity structures appear compact and symmetric, indicating stable vortex formation. As Br increases from 20% to 30%, the intensity and spatial extent of Ω_x increase, resulting in laterally expanded and more prominent vortical structures that reflect stronger rotational motion and elevated near-bed turbulence. These findings underscore the influence of blockage effects on near-bed vortex dynamics (Ω_x), with important implications for sediment transport, scour formation, and hydrodynamic forces on structures in confined channel environments.

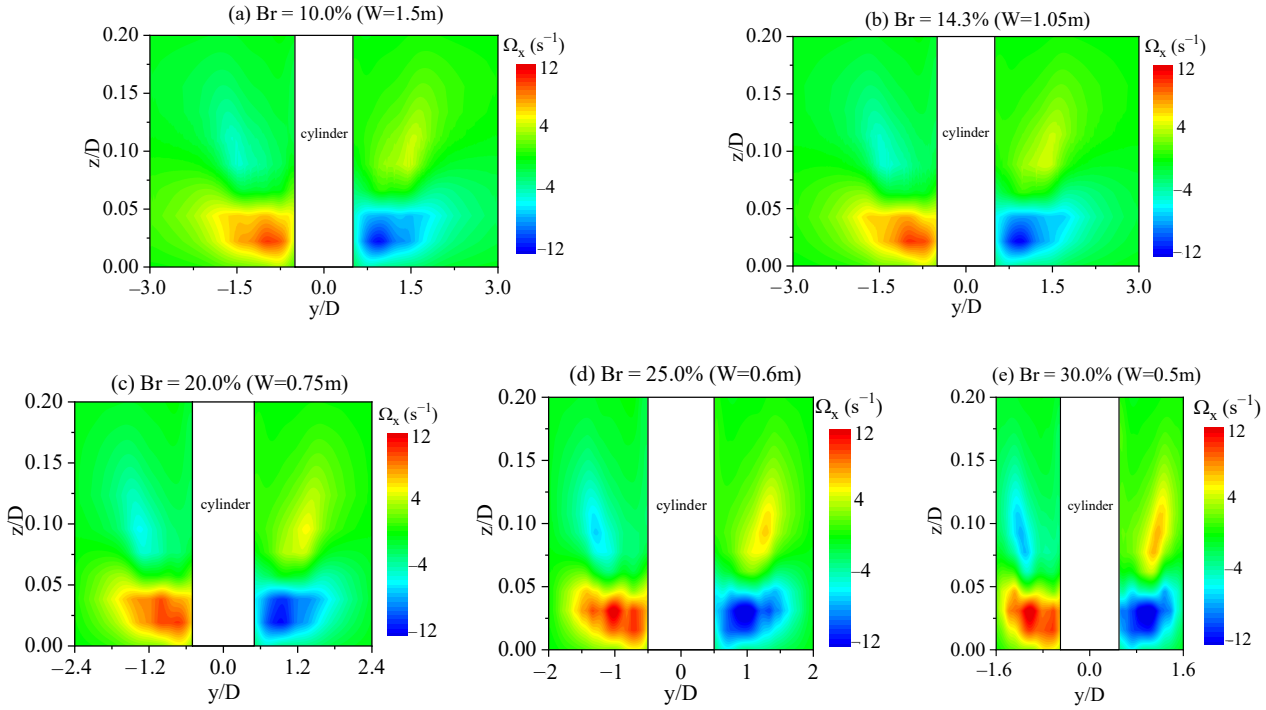

Figure 17. Vorticity distribution (Ω_x) on the y-z plane (x/D = 6.0) of the cylinder. (**a**) Br = 10%; (**b**) Br = 14.3%; (**c**) Br = 20%; (**d**) Br = 25%; (**e**) Br = 30%.

Building on these observations, Figure 18 summarizes the correlation between the maximum (red circles) and minimum (blue square) streamwise vorticity values (Ω_x). These values are measured at the cross-section through the cylinder center (y-z plane) at x/D = 6. The vorticity magnitudes exhibit a slight increase with Br values, ranging from Ω_{x_max} = 13.1 to 14.6 s^{-1} and Ω_{x_min} = −14 to −15 s^{-1}. The vorticity distribution remains symmetric on both sides of the cylinder, with the vortex cores (locations of peak vorticity) consistently located around $y/D = \pm 1.02$ and z/D = 0.03 across all cases. Although the channel side walls have a limited impact on the magnitude of Ω_x in the gap region, the emergence of secondary vortices opposing the main vortex becomes more evident as the channel narrows. This effect is particularly pronounced when $Br \geq 20\%$, as shown in Figure 17. These intensified vortices expand their influence area, leading to erosion not only at the base of bridge piers but also along the channel banks, contributing to bank instability and lateral scour.

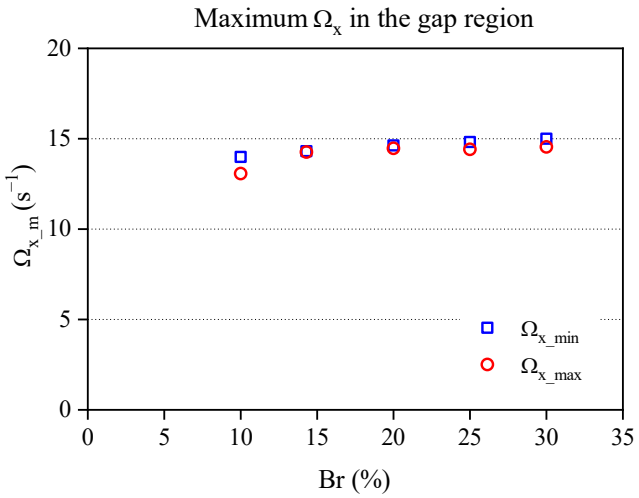

Figure 18. Maximum and minimum vorticity Ω_x on the y-z plane (x/D = 6.0) versus blockage ratio.

In addition to the streamwise (Ω_x) and vertical (Ω_y) vorticity components shown in the preceding figures, Figure 19 presents the time-averaged distribution of the spanwise vorticity (Ω_z) at a height of z/D = 0.05 for various *Br*. The Ω_z component is concentrated in the gap region between the cylinder and the channel wall, originating from the cylinder surface and extending downstream into the wake. The magnitude of Ω_z increases with *Br*, indicating intensified vortex shedding under more confined flow conditions. At *Br* = 25% and 30%, two secondary vortices emerge and align downstream along the channel wall, forming a nearly straight structure. In addition, due to the no-slip boundary condition at the lateral wall, the velocity at the channel wall is zero, while the adjacent flow in the gap region remains non-zero. This velocity gradient generates an additional shear-induced vortex near the channel wall, which enhances local spanwise rotation and contributes to the three-dimensional complexity of the wake. This near-wall vortex may further intensify lateral momentum transport and promote local scour along the channel boundary.

Figure 20 shows the variation in the maximum and minimum spanwise vorticity (Ω_z) at z/D = 0.05 across a range of *Br*. As *Br* increases from 10% to 30%, both Ω_{z_max} and Ω_{z_min} exhibit a consistent rise from approximately $\pm$15.0 s^{-1} to $\pm$18.2 s^{-1}. The locations of these peak values remain nearly constant at x/D = 6.1 and y/D = $\pm$0.54, indicating a persistent vortex formation zone near the cylinder. This trend reflects the intensification of shear layers within the narrowing gap caused by increased blockage, which enhances vorticity generation. The symmetrical growth of positive and negative vorticity suggests the development of stronger and more coherent rotational structures on both sides of the wake, thereby contributing to more complex flow dynamics at higher *Br* values.

As shown in the results above, although the effects of *Br* on vorticity values appear minor, their cumulative impact could influence long-term structural performance. Therefore, understanding the subtle variations in vorticity induced by blockage is essential for improving the reliability and durability of structures subjected to confined flow conditions. Overall, this insight highlights the importance of incorporating *Br* considerations into the design process to optimize performance and prevent potential structural failures over time, particularly in cases where $Br \geq 20\%$.

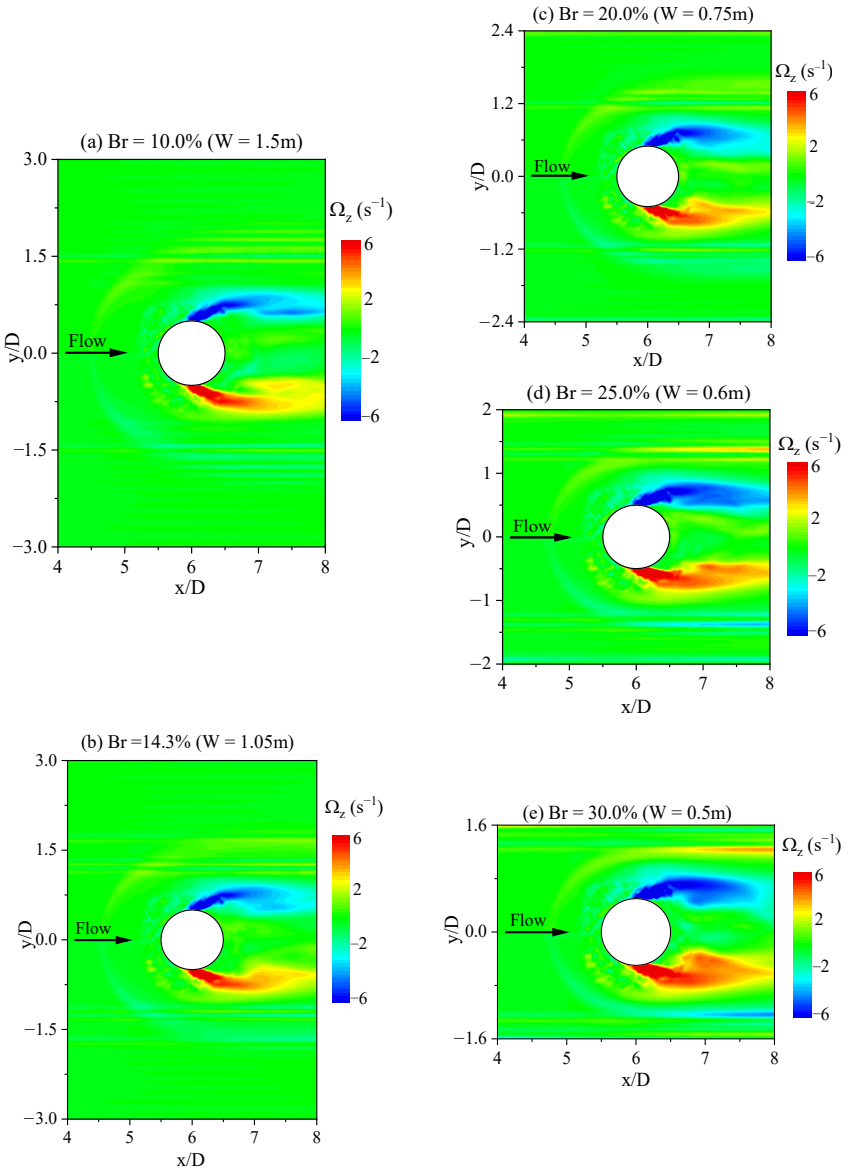

Figure 19. Distribution of the vorticity Ω_z on the x-y plane of the cylinder at height z/D = 0.05. (**a**) *Br* = 10%; (**b**) *Br* = 14.3%; (**c**) *Br* = 20%; (**d**) *Br* = 25%; (**e**) *Br* = 30%.

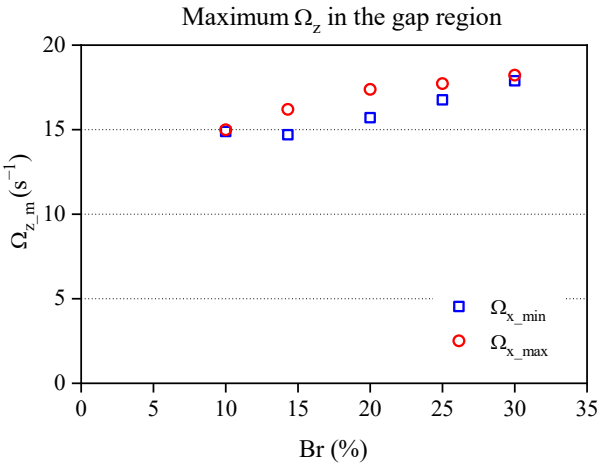

Figure 20. Maximum and minimum vorticity Ω_z on the x–y plane (at height z/D = 0.05) for different *Br*.

5. Conclusions

This study employed the LES model and VOF method to investigate the hydrodynamic forces and the vorticity distribution around a circular cylinder in a confined channel. The numerical model was validated against experimental data from [7], as detailed in Section 3. The numerical model was then utilized to investigate the impact of blockage on the vortex structure near the channel and hydrodynamic loading through a series of numerical simulations. The simulated results are as follows:

- The blockage ratio has a significant influence on the pressure and force characteristics around the cylinder. The changes in the upstream and circumferential pressure distributions, along with elevated drag coefficients, reflect the effect of flow confinement. At Br = 20–30%, amplified oscillations in the lateral force coefficient lead to higher C_{L_rms} and St values, highlighting the impact of blockage on hydrodynamic loading in confined channels.
- The vorticity analysis indicates that increasing Br intensifies near-wall vortex structures, particularly through elevated vertical (Ω_y), streamwise (Ω_x), and spanwise (Ω_z) vorticity components. As Br increases, the vorticity field becomes more dominant and spatially extensive, with Ω_x and Ω_z forming elongated structures and enhancing near-bed turbulence on the leeward side of the cylinder. These changes suggest that higher blockage ratios (Br = 20–30%) promote strengthening vortex activity near the bed, increasing the potential for local scour in narrow-channel conditions with erodible beds.

In conclusion, the present study confirms that $Br \geq 20\%$ significantly affects flow characteristics around a circular cylinder in narrow channels, including the upstream and circumferential pressure coefficients, drag coefficient, lateral force coefficient, and Strouhal number. The enhanced near-wall vortex structures and shear layers at higher Br contribute to increased vorticity magnitudes, with important implications for structural performance and erosion. These findings emphasize key design considerations for engineers, particularly regarding hydrodynamic forces acting on obstacles in confined environments. However, this study was conducted at a fixed Reynolds number, which limits its ability to capture Reynolds number-dependent flow phenomena such as transition to turbulence, scale separation in vortical structures, and increased flow unsteadiness. As such, future studies are recommended to investigate the effects of varying Reynolds numbers on hydrodynamic forces and vorticity distributions around a circular cylinder in confined channels, particularly at Br = 30%.

Author Contributions: Methodology, investigation, formal analysis, visualization, writing—original draft preparation, T.T.T.T.; conceptualization, funding acquisition, supervision, writing and editing the manuscript, C.-R.C.; methodology, software, T.-R.W. All authors have read and agreed to the published version of the manuscript.

Funding: This research was supported by the National Science and Technology Council, Republic of China, Taiwan, with grant no. 112-2221-E-008-024.

Data Availability Statement: The simulation data will be available on reasonable request to the first author.

Acknowledgments: The financial support from the Ministry of Science and Technology (MOST) of Republic of China, Taiwan, under grant no. MOST 112-2221-E-008-024, is gratefully appreciated.

Conflicts of Interest: The authors declare no conflicts of interest.

References

1. Brandimarte, L.; Paron, P.; Baldassarre, G.D. Bridge Pier Scour: A Review of Processes, Measurements and Estimates. *Environ. Eng. Manag. J.* **2012**, *11*, 975–989. [CrossRef]
2. Melville, B.; Coleman, S.E. *Bridge Scour*; Water Resource, LLC.: Highlands Ranch, CO, USA, 2000; ISBN 9781887201186.
3. Richardson, E.V.; Davis, S.R. *Evaluating Scour at Bridges*, 4th ed.; FHWA NHI 01-001 HEC-18; Federal Highway Administration (FHWA), U.S. Department of Transportation: Washington, DC, USA, 2001.
4. Wardhana, K.; Hadipriono, F.C. Analysis of Recent Bridge Failures in the United States. *J. Perform. Constr. Facil.* **2003**, *17*, 144–150. [CrossRef]
5. Imhof, D. *Risk Assessment of Existing Bridge Structures*; University of Cambridge: Cambridge, UK, 2004.
6. Zhang, G.; Liu, Y.; Liu, J.; Lan, S.; Yang, J. Causes and Statistical Characteristics of Bridge Failures: A Review. *J. Traffic Transp. Eng. (Engl. Ed.)* **2022**, *9*, 388–406. [CrossRef]
7. Dargahi, B. Experiments in Fluids The Turbulent Flow Field around a Circular Cylinder. *Exp. Fluids* **1989**, *8*, 1–12. [CrossRef]
8. Simpson, R.L. Junction Flows. *Annu. Rev. Fluid Mech.* **2001**, *33*, 415–443. [CrossRef]
9. Das, S.; Das, R.; Mazumdar, A. Vorticity and Circulation of Horseshoe Vortex in Equilibrium Scour Holes at Different Piers. *J. Inst. Eng. (India) Ser. A* **2014**, *95*, 109–115. [CrossRef]
10. Gautam, P.; Eldho, T.I.; Mazumder, B.S.; Behera, M.R. Experimental Study of Flow and Turbulence Characteristics around Simple and Complex Piers Using PIV. *Exp. Therm. Fluid Sci.* **2019**, *100*, 193–206. [CrossRef]
11. Olsen, N.R.B.; Melaaen, M.C. Three-Dimensional Calculation of Scour around Cylinders. *J. Hydraul. Eng.* **1993**, *119*, 1048–1054. [CrossRef]
12. Olsen, N.R.B.; Kjellesvig, H.M. Three-Dimensional Numerical Flow Modeling for Estimation of Maximum Local Scour Depth. *J. Hydraul. Res.* **1998**, *36*, 579–590. [CrossRef]
13. Torsethaugen, K. *Lokalerosjon ved Store Konstruksjoner*; SINTEF Report No. STF60A75055; The Norwegian Hydrotechnical Laboratory: Trondheim, Norway, 1975. (In Norwegian)
14. Tseng, M.H.; Yen, C.L.; Song, C.C.S. Computation of Three-Dimensional Flow around Square and Circular Piers. *Int. J. Numer. Meth. Fluids* **2000**, *34*, 207–227. [CrossRef]
15. Escauriaza, C.; Sotiropoulos, F. Reynolds Number Effects on the Coherent Dynamics of the Turbulent Horseshoe Vortex System. *Flow Turbul. Combust.* **2011**, *86*, 231–262. [CrossRef]
16. Kirkil, G.; Constantinescu, G. Effects of Cylinder Reynolds Number on the Turbulent Horseshoe Vortex System and near Wake of a Surface-Mounted Circular Cylinder. *Phys. Fluids* **2015**, *27*, 075102. [CrossRef]
17. Ranga Raju, K.G.; Rana, O.P.S.; Asawa, G.L.; Pillai, A.S.N. Rational Assessment of Blockage Effect in Channel Flow Past Smooth Circular Cylinders. *J. Hydraul. Res.* **1983**, *21*, 289–302. [CrossRef]
18. Davis, R.W.; Moor, E.F.; Purtell, L.P. A Numerical Experimental Study of Confined Flow around Rectangular Cylinders. *Phys. Fluids* **1984**, *27*, 40–59. [CrossRef]
19. Chu, C.R.; Chung, C.H.; Wu, T.R.; Wang, C.Y. Numerical Analysis of Free Surface Flow over a Submerged Rectangular Bridge Deck. *J. Hydraul. Eng.* **2016**, *142*, 108567. [CrossRef]
20. Chu, C.R.; Lin, Y.A.; Wu, T.R.; Wang, C.Y. Hydrodynamic Force of a Circular Cylinder Close to the Water Surface. *Comput. Fluids* **2018**, *171*, 154–165. [CrossRef]
21. Nguyen, Q.D.; Lei, C. Hydrodynamic Characteristics of a Confined Circular Cylinder in Cross-Flows. *Ocean Eng.* **2021**, *221*, 108567. [CrossRef]
22. Hurtado-Herrera, M.; Zhang, W.; Hammouti, A.; Pham, V.B.; Nguyen, K.D. Numerical Study of the Flow and Blockage Ratio of Cylindrical Pier Local Scour. *Appl. Sci.* **2023**, *13*, 11501. [CrossRef]
23. Lachaussée, F. Érosion et Transport de Particules au Voisinage d'un Obstacle. Ph.D. Thesis, Université Paris-Saclay, Paris, France, 2018.
24. Roulund, A.; Sumer, B.M.; Fredsøe, J.; Michelsen, J. Numerical and Experimental Investigation of Flow and Scour around a Circular Pile. *J. Fluid Mech.* **2005**, *534*, 351–401. [CrossRef]
25. Korzekwa, D.A. Truchas—A Multi-Physics Tool for Casting Simulation. *Int. J. Cast Met. Res.* **2009**, *22*, 187–191. [CrossRef]
26. Wu, T.R.; Vuong, T.H.N.; Lin, J.W.; Chu, C.R.; Wang, C.Y. Three-Dimensional Numerical Study on the Interaction between Dam-Break Wave and Cylinder Array. *J. Earthq. Tsunami* **2018**, *12*, 1840007. [CrossRef]
27. Chu, C.R.; Tran, T.T.T.; Wu, T.R. Numerical Analysis of Free-Surface Flows over Rubber Dams. *Water* **2021**, *13*, 1271. [CrossRef]
28. Deardorff, J.W. A Numerical Study of Three-Dimensional Turbulent Channel Flow at Large Reynolds Numbers. *J. Fluid Mech.* **1970**, *41*, 453–480. [CrossRef]
29. Pop, S.B. *Turbulent Flows*; Cambridge University Press: Cambridge, UK, 2000; ISBN 978-0-5215-9886-6.
30. O'Neil, J.; Meneveau, C. Subgrid-Scale Stresses and Their Modelling in a Turbulent Plane Wake. *J. Fluid Mech.* **1997**, *349*, 253–293. [CrossRef]

31. Cabot, W.; Moin, P. Approximate Wall Boundary Conditions in the Large Eddy Simulation of High Reynolds Number Flow. *Flow Turbul. Combust.* **1999**, *63*, 269–291. [CrossRef]
32. Smagorinsky, J. General Circulation Experiments with the Primitive Equation I: The Basic Experiment. *Mon. Weather Rev.* **1963**, *91*, 99–164. [CrossRef]
33. Rodi, W.; Constantinescu, G.; Stoesser, T. *Large-Eddy Simulation in Hydraulics*; CRC Press: Boca Raton, FL, USA, 2013; ISBN 978-0-3675-7638-7.
34. Huynh, L.E.; Chu, C.R.; Wu, T.R. Hydrodynamic Loads of the Bridge Decks in Wave-Current Combined Flows. *Ocean Eng.* **2023**, *270*, 113520. [CrossRef]
35. Truong, N.M.; Wu, T.R.; Chu, C.R.; Wang, C.Y. A Numerical Study of Plunging Breakers in the Nearshore Area under the Influence of Wind. *Ocean Eng.* **2024**, *312*, 119171. [CrossRef]
36. DeLong, M. *Two Examples of the Impact of Partitioning with Chaco and Metis on the Convergence of Additive-Schwarz Preconditioned FGMRES*; Los Alamos National Laboratory: Los Alamos, NM, USA, 1997.
37. Hirt, C.W.; Nichols, B.D. Volume of Fluid (VOF) Method for the Dynamics of Free Boundaries. *J. Comput. Phys.* **1981**, *39*, 201–225. [CrossRef]
38. Iqbal, S.; Dissanayaka, K.D.C.R.; Tanaka, N. Numerical Modeling and Validation of Dike-Induced Water Flow Dynamics Using OpenFOAM. *ISH J. Hydraul. Eng.* **2024**, *30*, 559–573. [CrossRef]
39. Anjum, N.; Iqbal, S.; Pasha, G.A.; Tanaka, N.; Ghani, U. Optimizing Coastal Forest Arrangements for Tsunami Flow Dynamics Using a Three-Dimensional Approach. *Phys. Fluids* **2025**, *37*, 035197. [CrossRef]
40. Piomelli, U.; Chasnov, J.R. *Chapter 7 Large-Eddy Simulations: Theory and Applications*; Kluwer Academic Publishers: Dordrecht, The Netherlands, 1996.
41. Salim, S.M.; Cheah, S.C. Wall Y+ Strategy for Dealing with Wall-Bounded Turbulent Flows. In Proceedings of the International MultiConference of Engineers and Computer Scientists, Hong Kong, China, 18–20 March 2009; Newswood Ltd.: Hong Kong, China; International Association of Engineers: Hong Kong, China, 2009; Volume II, p. 2210.
42. Larsson, J.; Kawai, S. Wall-Modeling in Large Eddy Simulation: Length Scales, Grid Resolution and Accuracy. *Cent. Turbul. Res. Annu. Res. Briefs* **2010**, 39–46.
43. Hoerner, S.F. Fluid Dynamic Drag: Theoretical, Experimental and Statistical Information. In *Hoerner Fluid Dynamics*; Hoerner Fluid Dynamics: Bakersfield, CA, USA, 1965.
44. Achenbach, E. Distribution of Local Pressure and Skin Friction around a Circular Cylinder in Cross-Flow up to Re = 5×10^6. *J. Fluid Mech.* **1968**, *34*, 625–639. [CrossRef]
45. Blevins, R.D. *Applied Fluid Dynamics Handbook*; Van Nostrand Reinhold Co.: New York, NY, USA, 1984.
46. Roshko, A. *On the Drag and Shedding Frequency of Two-Dimensional Bluff Bodies*; Government Printing Office: Washington, DC, USA, 1954.
47. Schlichting, H. *Boundary Layer Theory*, 7th ed.; McGraw-Hill Book Company: New York, NY, USA, 1979.
48. Achenbach, E.; Heinecke, E. On Vortex Shedding from Smooth and Rough Cylinders in the Range of Reynolds Numbers 6×10^3 to 5×10^6. *J. Fluid Mech.* **1981**, *109*, 239–251. [CrossRef]
49. Surry, D. Some Effects of Intense Turbulence on the Aerodynamics of a Circular Cylinder at Subcritical Reynolds Number. *J. Fluid Mech.* **1972**, *52*, 543–563. [CrossRef]
50. Richter, A.; Naudascher, E. Fluctuating Forces on a Rigid Circular Cylinder in Confined Flow. *J. Fluid Mech.* **1976**, *78*, 561–576. [CrossRef]
51. Norberg, C. Fluctuating Lift on a Circular Cylinder: Review and New Measurements. *J. Fluids Struct.* **2003**, *17*, 57–96. [CrossRef]
52. Baker, C.J. The Laminar Horseshoe Vortex. *J. Fluid Mech.* **1979**, *95*, 347–367. [CrossRef]